Manganese carbonate formation from amorphous and nanocrystalline precursors: Thermodynamics and geochemical relevance

A.V. Radha and Alexandra Navrotsky *

Peter A. Rock Thermochemistry Laboratory and NEAT ORU (Nanomaterials in the Environment, Agriculture, and Technology, Organized Research Unit), University of California Davis, One Shields Avenue, Davis, CA 95616, USA

Revision 1

*Corresponding author: anavrotsky@ucdavis.edu

ABSTRACT

The thermodynamic stabilities of different manganese carbonate phases at ambient conditions were determined by acid solution and water adsorption calorimetry. Amorphous manganese carbonate precursor provides a low energy pathway for $MnCO_3$ crystallization analogous to that observed in (Ca-Mg-Fe)CO_3 systems where crystallization enthalpies appear to be controlled by cation size (become less exothermic with increase in ionic radius). The surface energy of nanophase $MnCO_3$ (0.64 ± 0.08 J/m^2 for hydrous and 0.94 ± 0.12 J/m^2 for anhydrous surface) is lower than that of nano-calcite and $MnCO_3$ binds surface water less strongly (-66.6 ± 2.9 kJ/mol) than calcite (-96.26 ± 0.96 kJ/mol). This probably reflects the greater basicity of CaO compared to MnO. Substantial particle size driven shifts in the $MnCO_3$ - manganese oxide Eh - pH and oxygen fugacity-CO_2 fugacity diagrams were calculated using the measured surface energies. These shifts expand the stability field of hausmannite, Mn_3O_4, in both aqueous and anhydrous environments. The particle size driven (caused by differences in surface energy) shifts in oxidation potential (Eh, oxygen fugacity) and pH of phase boundaries could affect

stability and electrochemical and catalytic properties and hence influence geochemical and technological processes. Manganese oxides (mainly hausmannite) dominate at the nanoscale in aerated environments, while manganese carbonate is favored in coarse grained materials and reducing environments. In supercritical CO_2, the expansion of the $MnCO_3$ stability field leads to significant reduction of the Mn_3O_4 stability field.

Keywords: $MnCO_3$ (rhodochrosite) formation, crystallization enthalpy, surface energy, Eh/pE-pH diagram, CO_2 sequestration,

INTRODUCTION

Manganese carbonate minerals play a vital role in manganese geochemistry by regulating Mn(II) mobility and heavy metal transport, and in the carbon cycle by trapping CO_2 through mineralization (Bourg and Bertin 1994; Goren et al (2012); Pedersen and Price 1982; Schaef et al. 2009, 2010). Mn substituted calcite phases were observed in pilot studies on the reactivity of different basalt samples obtained from sites in the United States, India, and South Africa with aqueous dissolved CO_2 and CO_2–H_2S mixtures under supercritical CO_2 (Schaef et al. 2009, 2010). $MnCO_3$ is also used as a cost effective and environmentally friendly catalyst support, water treatment agent, and precursor for synthesis of metal oxides for lithium-ion battery materials (Cui et al. 2009; Takahara et al. (2012); Wang and Ao 2007; Yang et al. 2007). Recently, advancements in synthetic strategies have led to the development of multifunctional nano/microporous manganese carbonate composites with porous surfaces having potential in drug delivery, protein encapsulation, biosensing, and as antimicrobial agents (Peng et al. 2011; Qi et al. 2010; Wang et al. 2009; Zhang et al. 2009) as well as

promising, less expensive, Li-ion battery anode materials (Aragón et al. 2007, 2011; Mirhashemihaghighi et al. 2012).

$MnCO_3$ minerals are found in anaerobic soils and marine sediments, hydrothermal veins and sporadically in high temperature metasomatic deposits as crystalline $MnCO_3$ (rhodochrosite) or as solid solution with other carbonate minerals with rhombohedral calcite-type structure (Goren et al. (2012); Pedersen and Price 1982). Rhodochrosite ($MnCO_3$) crystal growth kinetic studies suggest that its growth depends on the chemical speciation of the mineral surface (Sternbeck 1997). Surface potential studies using Kelvin probe electron force microscopy indicate surface heterogeneity due to growth of thin films of manganese oxide nanostructures (Kendall et al. 2008; Na et al. 2007; Na and Martin 2009). These thin films alter crystal growth, reactivity, and surface electrical properties of the less reactive rhodochrosite surface by transforming it into a surface with regions of strongly reactive sites. Analogous phase transformations in other M-O (M = Fe, Mn and Co) systems have been shown to have thermodynamic underpinnings due to surface energy driven shifts in redox equilibria at the nanoscale (Birkner and Navrotsky 2012; Navrotsky et al. 2010).

There is growing evidence that calcium carbonate nucleation and growth takes place not only by classical nucleation system (De Yoreo and Vekilov 2003; De Yoreo et al. 2009; Hu et al. 2012) but also by non-classical mechanisms through prenucleation clusters (0.2 to 2 nm size), and liquid-like metastable amorphous, nanophase and mesocrystal precursors in the early stages (Bewernitz et al. 2012; de Yoreo et al. 2007; Fernandez-Martinez et al. 2013; Gebauer and Coelfen 2011; Gebauer et al. 2008; Raiteri and Gale 2010; Tribello et al. 2009; Wallace et al. 2013; Wolf et al. 2011). Our previous thermodynamic studies suggest that the early stage amorphous and nanophase precursors provide a low energy pathway for carbonate mineralization in (Ca-Mg-Fe)CO_3 systems (Forbes et al. 2011; Radha et al. 2012; Radha et al. 2010; Sel et al. 2012). To investigate particle size driven energy

crossovers in $CaCO_3$ Forbes et al., (2011) recently determined the surface energy of nanophase calcite using acid solution calorimetry. Analogous data are not available for manganese carbonates. However, the structure and phase evolution in the $CaCO_3$-$MnCO_3$ solid solution system have been investigated extensively to understand the mixing thermodynamics and formation of intermediate ordered dolomite-type phases ($Ca_{0.5}Mn_{0.5}CO_3$, kutnahorite) (Capobianco and Navrotsky 1987; Goldsmith and Graf 1957; Katsikopoulos et al. 2009; McBeath et al. 1998; Pedersen and Price 1982; Wang et al. 2011).

In this work, we synthesized and measured the energetics of amorphous and nanophase manganese carbonates to understand their influence on crystal growth, surface reactivity and nanoscale properties of $MnCO_3$. First, we synthesized amorphous manganese carbonate and measured its crystallization enthalpy using isothermal acid solution calorimetry. To understand the contribution of molecular level surface interactions during manganese carbonate formation and nanoscale thermodynamic effects on its properties, we measured the energetics of nanophase manganese carbonate and determined its surface energy using acid solution and water adsorption calorimetric techniques. Finally, we evaluated the particle size dependent thermodynamic influence on manganese carbonate formation from manganese oxide precursors by constructing Eh(pE)-pH and oxygen-CO_2 fugacity diagrams and analyzed possible $MnCO_3$ formation during CO_2 sequestration.

MATERIALS AND METHODS

Sample Syntheses

Reagent grade $MnSO_4 \cdot 2H_2O$, Na_2CO_3 and $NaHCO_3$ were used for all syntheses. All solutions were prepared using ultra-pure water (resistivity = 18 Mohm.cm at 25 °C) from a Simplicity water

purification system. Nitrogen gas was bubbled through all solutions for at least 30 minutes to remove any dissolved oxygen.

Amorphous manganese carbonate (AMnC): Samples were synthesized by modifying the earlier synthetic approach for amorphous carbonates (Koga et al. 1998). AMnC was precipitated by adding 150 ml 0.02 M $MnSO_4$ solution to 150 ml of 0.02 M Na_2CO_3 solution with constant stirring and nitrogen bubbling. Both solutions were cooled in a refrigerator at 4 °C prior to mixing to minimize the crystallization. The precipitate was immediately filtered under vacuum, washed with acetone several times and vacuum dried overnight at 25 °C.

Nanocrystalline manganese carbonate (NMnC): NMnC samples were synthesized by adding 200 ml of 0.1 M $MnSO_4$ solution to 200 ml of sodium carbonate-bicarbonate buffer (pH = 9) solution at 25 °C. The solution was split into two equal parts immediately after mixing and then aged separately at room temperature and 85 °C in an oven. After aging, solutions were filtered separately under vacuum, washed with acetone several times and vacuum dried overnight at 25 °C. The samples were prepared in 4 separate batches and aged at ambient and 85 °C for 0, 1.0, 2.5 and 5.0 h. A 30 ml sample of the above precipitated solution was hydrothermally treated at 160 °C in a 50 ml capacity Teflon-lined autoclave for 18 h to obtain a bulk $MnCO_3$ sample with BET particle size above 100 nm.

Both amorphous and nanophase manganese carbonate phases were hydrated with composition $MnCO_3 \cdot nH_2O$ (see Tables 1 and 2). All dried samples were first equilibrated in air for 24 h in the calorimetry laboratory, continually maintained at 24 ± 0.5 °C and 50 ± 5 % relative humidity, and then stored in screw capped vials in a desiccator with drierite desiccant. All sample characterization and calorimetric measurements on amorphous samples were carried out within a week to minimize any changes due to sample aging. The water contents of the samples were determined from the first weight loss step (ambient to 200 °C) in the thermogravimetric analysis (TGA) curve.

114

115 **Sample characterization**

116 Powder X-ray diffraction patterns of all samples were collected using a Bruker AXS D8
117 Advance diffractometer with a zero background sample holder and LynxEye solid state detector (Cu
118 K_α radiation; step size = 0.01 º and a collection time = 0.5-2 s/step). Phase identification and
119 crystallite size analysis by whole pattern fitting were performed using JADE 8.0 software. The
120 crystallite size from the XRD profiles were determined by whole pattern fitting based on the Scherrer
121 equation with spherical particle shape. A Netzsch STA 449 system was used to carry out
122 thermogravimetric analysis and differential scanning calorimetry (TGA/DSC) measurements in a
123 platinum crucible with argon flow from 30 to 1200 °C at 10 °C/min. The gases evolved during thermal
124 analysis were examined using a Bruker Equinox 55 FTIR spectrometer (range 400 - 4000 cm^{-1})
125 coupled to the Netzsch STA 449 system by a transfer line heated to 150 °C to confirm the loss of H_2O
126 and CO_2 during TG-DSC runs. The surface area of the samples (degassed at 150 °C for 2 hours) was
127 characterized by nitrogen adsorption measurements using the Brunauer-Emmett-Teller (BET) method
128 with a Micromeritics ASAP 2020 instrument. A five point N_2 adsorption isotherm was collected in
129 triplicate for 0.1 g of each sample in the P/P_0 relative pressure range of 0.05 - 0.3, where P_0 is the
130 saturation pressure at -196 °C. Scanning electron microscopy *(SEM)* studies were conducted to
131 confirm particle size on a Philips FEI XL30-SFEG high resolution scanning electron microscope at an
132 accelerating voltage of 5 kV. For analysis by scanning electron microscopy, powder samples were
133 ultrasonicated in ethanol, drop-cast onto copper tape, and sputter coated with gold.

134

135 **Calorimetry:**

The instrument and methodology used for isothermal acid solution calorimetry for carbonates have been described earlier (Forbes et al. 2011; Radha et al. 2010). A CSC 4400 isothermal microcalorimeter with mechanical stirring was used to measure the enthalpies of solution of samples at 26 °C. Typically a ~5 mg sample pellet was dropped into 5 N HCl solvent (~25 g) and the heat flow (μJ/s) as a function of time gives a calorimetric signal. Measured enthalpies of solution are given in Tables 1 and 2.

A Micromeritics ASAP 2020 gas adsorption analyzer coupled with a Setaram Sensys Calvet microcalorimeter was used for simultaneous accurate water dosing to the sample and measurement of enthalpy of adsorption for each incremental dose of water (Ushakov and Navrotsky 2005). Each water dose (~1-2 micromoles) generates a distinct calorimetric peak and the area under the peak gives the differential enthalpy of adsorption. All chemically adsorbed water generates an adsorption peak with differential enthalpy more negative than the condensation enthalpy of water at 25 °C (-44 kJ/mol). The sum of the differential enthalpies of adsorption divided by the total water up to this coverage gives the integral enthalpy ($\Delta H_{adsH2Ovapor}$). At least 3 runs were done on each sample after degassing at 150 °C for 2 h between the measurements. A blank with the empty tube was run to correct the above data for water adsorbed on the forked tube wall.

RESULTS

Crystallization energy of amorphous manganese carbonate (AMnC):

The absence of any Bragg reflections in the powder XRD patterns of the AMnC samples (Fig. 1a) confirms the formation of X-ray amorphous samples. The X-ray patterns of the same dry AMnC samples stored for 40 days showed sharp reflections of a calcite-like phase. This indicates that the amorphous $MnCO_3$ is metastable and slowly crystallizes to rhodochrosite (see Fig 1a). Therefore, we

159 measured the energetics on two freshly prepared AMnC samples (AMnC I and II) to minimize any
160 aging as well as crystallization effects.

161 The thermal decomposition of manganese carbonate is complex due to the formation of various
162 interconvertible manganese oxide phases in different environments (inert or oxidizing) and
163 temperatures (Seguin 1972). In our experiments, the single step decomposition with 38.5% TG weight
164 loss (Fig. SI-1a in supporting information) and the XRD pattern of the decomposed TG products of
165 crystalline bulk $MnCO_3$ confirm the formation of MnO in an Ar atmosphere. At higher temperature,
166 the liberated CO_2, if not flushed out, further reacts with MnO to form Mn_3O_4 and CO (Seguin 1972).
167 The TGA profile of AMnC sample on heating in Ar show that the first weight loss step (30 - 200 °C)
168 corresponds to sample dehydration and they are different for AMnC I and II samples (see Table 1)
169 and The second weight loss is due to decomposition of $MnCO_3$ to MnO (See Fig SI-1b in supporting
170 information). The FTIR spectra of the gases evolved during TG-DSC measurements further confirm
171 the loss of H_2O and CO_2 at the first and second TGA weight loss steps. The DSC profile of AMnC
172 (Fig. SI-1b in supporting information) shows multiple thermal events similar to those observed in
173 amorphous iron (II) carbonate (Sel et al. 2012). The first endothermic DSC peak (30 - 200 °C)
174 corresponds to loss of water. The second step (200 - 420 °C) shows several thermal events with
175 simultaneous crystallization (exothermic) and decomposition (endothermic) to MnO occurring around
176 ~ 400 °C.

177 The measured enthalpies of solution in 5 M HCl at 26 °C of two freshly prepared amorphous
178 samples and bulk crystalline $MnCO_3$ are given in Table 1. Amorphous manganese carbonate readily
179 dissolved in 5M HCl to form a very pale pink solution containing Mn(II) ions. The measured
180 exothermic solution enthalpies are used in thermochemical cycle-I in Table 3 to arrive at the
181 crystallization enthalpies of amorphous carbonate samples. The calculated crystallization enthalpies of

two freshly prepared amorphous samples (AMnC I and II) agree with each other within the uncertainties of measurements and correspond to -32.44 ± 0.71 kJ/mol. Although the SEM image of (Fig SI-2 in supporting information) suggest the nanoparticlulate (25-50 nm) nature of AMnC samples, no correction for the surface energy contribution to the crystallization enthalpy has been made because the difference in surface energy between amorphous and crystalline $MnCO_3$ is not known. The exothermic crystallization of AMnC confirms that amorphous $MnCO_3$ is a metastable phase. It could provide a low energy pathway for crystalline rhodochrosite mineralization analogous to other carbonate systems with Ca, Mg and Fe cations (Forbes et al. 2011; Radha et al. 2012; Radha et al. 2010; Sel et al. 2012).

Surface energy of nanophase manganese carbonate (NMnC)

The phase identification of nanophase and bulk manganese carbonate samples by powder XRD (see Fig. 1b) confirms the formation of rhodochrosite (PDF # 65-1302) with calcite-type structure. A typical TG-DSC curve for NMnC shows just two-step thermal reactions due to dehydration and decomposition of $MnCO_3$ to MnO and CO_2 (See Fig SI-1c). The water contents per mole of $MnCO_3$ in NMnC samples (calculated from TGA first weight loss step) were smaller than that of the amorphous phase. Further, the absence of any sharp exothermic crystallization DSC peak confirms the absence of significant residual amorphous phase in NMnC samples.

Table 2 summarizes the particle size analysis of NMnC samples. The crystallite size and the corresponding calculated surface areas from the XRD profiles range from 9.1 to 58.9 nm and 178 to 27.5 m^2/g, respectively. The BET surface area of the NMnC samples obtained from the nitrogen adsorption isotherm range from 84.5 ± 0.24 to 7.5 ± 0.2 m^2/mol. The measured BET surface areas are smaller than the values calculated from the XRD particle size (Table 2). The particle sizes estimated

from SEM studies (Fig SI-2) show a wide range of particle size distribution from 32 ± 2 to 144 ± 10 nm (corresponding to surface areas of 50.7 to 11.3 m^2/g) and are much higher than values from the XRD and BET measurements. These differences among X-ray, BET and SEM estimates of surface area and particle size are consistent with extensive particle agglomeration. This could occur on dehydration during sample preparation using gold sputter coating or during SEM measurement under high vacuum. Such discrepancies were also observed in our earlier study on surface energy of nanophase calcite (Forbes et al. 2011) that concluded that surface area determination is best performed using BET analysis. Since calcite and rhodochrosite are similar in structure, one could argue that conclusions deduced for calcite would apply to $MnCO_3$ as well. Therefore, we used the surface area obtained from BET analysis in calculation of the surface energy of nanophase manganese carbonate.

Figure 2 shows the adsorption enthalpies for individual water vapor doses (differential enthalpies) as a function of water coverage on the NMnC surface (H_2O per nm^2). The water coverage up to the water condensation point corresponds to the chemisorbed water and the average coverage from 2 runs on NMnC surface is 9 ± 1 H_2O/nm^2. The remaining water (with a differential enthalpy -44 kJ/mol) is physically adsorbed water. The calculated integral enthalpy ($\Delta H_{adsH2O\text{-}vapor}$) value for NMnC surface is -66.6 ± 2.9 kJ/mol and corresponds to the average enthalpy of chemisorbed water vapor at 25 °C. The enthalpy of chemisorption for liquid water ($\Delta H_{chemiads\text{-}liquid}$) was calculated by removing the contribution of enthalpy of condensation of water vapor at 25 °C (-44 kJ/mol) from the integral enthalpy ($\Delta H_{adsH2O\text{-}vapor}$). The enthalpies of solution (ΔH_{soln}) for NMnC samples measured by isothermal calorimetry in 5 M HCl at 26 °C range from -19.2 ± 0.4 to -25.5 ± 0.6 kJ/mol (Table 2). All NMnC samples are hydrated and the corrected enthalpies ($\Delta H_{sol\text{-}corr;\ nano}$) are obtained by subtracting the contribution of adsorbed water from enthalpies of solution (ΔH_{soln}). The surface enthalpy (γ in J/m^2) of nanophase manganese carbonate for a given surface area (SA in m^2/mol) is the excess

enthalpy of nanophase with respect to bulk ($\Delta H_{sol\text{-}bulk} = \Delta H_{sol\text{-}corr;\ nano} + SA^*\gamma$). Any particle size above 100 nm can be treated as a bulk sample in terms of enthalpy because the product of surface area times surface energy gives an effect within experimental error of calorimetric measurements.

Figure 3 shows the water-corrected solution enthalpies plotted against the surface area obtained from BET analysis. The solution enthalpies are corrected for contribution associated with surface water as physically ($\Delta H_{sol\text{-}corr\text{-}physi}$) and chemically ($\Delta H_{sol\text{-}corr\text{-}chemi}$) adsorbed water (see thermochemical cycles given in Table 3) and they correspond to hydrous and anhydrous surfaces, as discussed in earlier papers (Birkner and Navrotsky 2012; Forbes et al. 2011; Ma et al. 2011; Navrotsky 2009). The data points for both hydrous and anhydrous surfaces each follow linear trends with goodness of fit (R^2) values 0.87 and 0.91. The negative of the slopes of the linear fits correspond to the surface enthalpies. Any substantial contribution of interface enthalpy due to sample agglomeration would lead to non-linear trends and thus this effect seems to be insignificant. The surface enthalpies for hydrous and anhydrous nano-manganese carbonate surfaces are 0.64 ± 0.08 J/m^2 and 0.94 ± 0.12 J/m^2 respectively. These surface enthalpy values are also approximations to surface energy and surface free energy since the contribution of excess volume (PV term) and surface entropy term ($T\Delta S$) are small (Smith et al. 2009; Wang et al. 2004). Duckworth et al. (2004) report the only other available calculated surface energy (0.442 J/m^2) using molecular dynamics simulation studies. The measured surface energy is larger than that from computational modeling of idealized crystallite surfaces but is within the range of those measured for many oxides (Navrotsky 2009). The surface enthalpy of $MnCO_3$ (0.9 ± 0.1 J/m^2) is lower than that of calcite (1.9 ± 0.2 J/m^2), which suggests the surface interactions of $MnCO_3$ are weaker than those of the calcite surface. Furthermore, the less exothermic water adsorption enthalpy of $MnCO_3$ (-66.6 ± 2.96 kJ/mol) compared to calcite (-96.26 ± 0.96 kJ/mol) supports weaker interaction on the $MnCO_3$ surface.

251 .

252 ## DISCUSSION

253 ### Pattern of crystallization energetics in amorphous carbonates

254 To better understand the driving force behind the crystallization of carbonates, we compare the
255 crystallization energetics of amorphous Ca, Mg, Fe and Mn carbonates as a function of cation ionic
256 radius in Table 1. As noted in our earlier study (Sel et al. 2012), the crystallization enthalpies become
257 less exothermic with an increase in cation radius. Interestingly, isostructural crystalline carbonate
258 minerals also show a similar linear dependence of physical (hardness and density) and spectroscopic
259 (shifts in IR peak positions) properties on cation radius (Railsback 1999). However, geochemical
260 properties such as solubility and distribution coefficients are shown to be controlled by the degree of
261 cation fit in the crystal structure (Railsback 1999). Our current study illustrates the influence of cation
262 radius on the thermodynamics of carbonate crystallization. In order to obtain a fundamental
263 understanding of this trend, there needs to be a detailed structural analysis of amorphous phases in the
264 (Ca-Mg-Fe-Mn)CO_3 system and their M-O bonding environment. This could help link
265 thermodynamics, kinetics, and physical properties.

266

267 ### Surface energy effects on manganese carbonate formation from manganese oxide precursors

268 To understand nanoscale effects on manganese carbonate formation from manganese oxide in
269 aqueous medium, we constructed Eh-pH diagrams (Figure 4) for bulk and 10 nm particles using
270 surface energies (hydrous) of nano-$MnCO_3$ (this study) and nano-Mn_3O_4 (Birkner and Navrotsky
271 2012) with aqueous Mn^{2+} (10^{-6} M) species for a CO_2 partial pressure corresponding to sea level air
272 ($P_{CO2} = 10^{-3.5}$ atm; T = 25 °C) and supercritical CO_2 (P_{CO2} = 72.9 atm; T = 31.25 °C). $MnCO_3$ exists
273 only as rhodochrosite therefore one cannot expect any particle size driven shifts in surface energy

related to polymorphic phase transformation. Also, for many oxides (Navrotsky 2009, 2011; Navrotsky et al. 2010) the excess enthalpy measured directly by calorimetry remains constant within experimental error (data fall on a straight line) down to particle sizes near 5-10 nm. For nanophase Mn minerals, all three phase boundaries show some particle size induced shifts (dashed lines in Fig 4) from the corresponding bulk phase boundaries (solid lines in Fig. 4), illustrating the surface energy driven effects on both acid-base and redox equilibria (see Tables SI-1 and SI-2 for thermodynamic data and chemical half reactions). The shifts in acid-base equilibria of the Mn^{2+}/nano$MnCO_3$ and Mn^{2+}/nanoMn_3O_4 phase boundaries toward higher pH confirm that nanophase minerals are metastable and therefore more soluble than bulk minerals. The nanophase Mn_3O_4/$MnCO_3$ phase boundary shifts suggest the expansion of the hausmannite, Mn_3O_4 stability field compared to bulk due to the surface energy contributions of nano Mn_3O_4 (0.96 ± 0.08 J/m^2) and $MnCO_3$ (0.64 ± 0.08 J/m^2) phases. For the Mn_3O_4/$MnCO_3$ anhydrous system, the oxygen - CO_2 fugacity diagrams at 25 and 100 °C (Fig. 5) indicate that both bulk and nano $MnCO_3$ (10 nm size) stability fields expand with an increase in CO_2 partial pressure (Reaction 4 in Table SI-2 in supporting information). High temperature favors the oxidation reaction as evidenced by the shifts in Mn_3O_4/$MnCO_3$ boundaries (expansion of Mn_3O_4 field) for bulk and nano to a lower oxygen fugacity region at 100 °C.

In contrast to the Mn-O system (Birkner and Navrotsky 2012), the size driven shifts in the Mn_3O_4/ $MnCO_3$ equilibrium in both Eh - pH and oxygen - CO_2 fugacity diagrams favor the formation of Mn_3O_4 over $MnCO_3$, even though Mn_3O_4 has the higher surface energy. This is because the surface energies of both phases are fairly similar and the total surface energy contributions of Mn_3O_4 and $MnCO_3$ phases in 1:3 molar ratio for the phase boundary reaction (see reactions in Table SI-2). This drives the formation of high surface energy Mn_3O_4 phase over $MnCO_3$, which leads to an expansion of the Mn_3O_4 stability field. These results demonstrate that at a redox interface, precipitation and

297 dissolution of Mn phases are controlled not only by redox potential of bulk phases but also by changes
298 in particle size driven surface energy effects, with manganese oxides dominating in nanoparticles in
299 oxidizing environments, but manganese carbonate dominating in bulk samples under reducing
300 conditions.

301 In supercritical CO_2, both Eh-pH and oxygen fugacity diagrams indicate the expanded stability
302 field for manganese carbonate formation. In supercritical CO_2 conditions (P_{CO2} = 72.9 atm; T =
303 31.25 °C), the effect of this modest pressure on surface enthalpy would be through a $P\Delta V$ term in
304 supercritical CO_2 conditions, where ΔV is the excess surface volume. There are no data for this but,
305 given the modest pressure used, it can not be a significant effect. In supercritical CO_2-H_2O fluid (Fig.
306 4b), both bulk and nano Mn_3O_4/$MnCO_3$ phase boundaries are pushed to higher Eh (more oxidizing)
307 and lower pH regions. This expansion of the carbonate stability field favors $MnCO_3$ formation at
308 lower pH (pH ~ 6 for bulk and pH ~ 7 for nano) leading to substantial reduction in the hausmannite
309 stability field. A significant expansion of the $MnCO_3$ field around CO_2 fugacity of 1.86 corresponding
310 to supercritical carbon dioxide (73 atm) in Figure 5 suggests its favorable formation in anhydrous
311 medium as well.
312

313 **IMPLICATIONS**

314 The mechanism of manganese carbonate formation is complex as it forms under reducing
315 conditions in anoxic organic rich sediments or by early diagenetic and biogeochemical processes, such
316 as microbial sulfate and MnO_2 reduction that facilitate Mn^{2+} formation (Frankel and Bazylinski 2003;
317 Gingele and Kasten 1994; Goren et al. (2012); Pedersen and Price 1982). A time-resolved X-ray
318 diffraction analysis of a bio-mediated enzymatic mineral reaction showed the systematic crystal
319 structure evolution from birnessite to hausmannite (Mn_3O_4) and finally to nanocrystalline

320 rhodochrosite through intermediate phases with a collapsing interlayer structure (Fischer et al. 2008).
321 Our study provides the thermodynamic basis for such structural evolution by illustrating the existence
322 of low energy pathways involving metastable amorphous and nano precursors for $MnCO_3$ precipitation.
323 This could be relevant to rhodoschrosite formation during biologically induced mineralization as well
324 as in anoxic organic rich sediments. Furthermore, the shifts in Eh (oxidation potential) with particle
325 size could affect electrochemistry and catalytic properties of these materials and hence influence their
326 geochemistry as well as various industrial applications.

327 Manganese carbonate is usually found as coarse deposits in various geochemical environments.
328 In marine environments, increase in grain size (with associated larger pore spaces) is found to be a
329 prerequisite for authigenic Mn-carbonate formation (Pedersen and Price 1982). Mn oxide minerals
330 typically occur as poorly crystalline fine grained (10 - 100 nm) brown-black masses or coatings and
331 are formed by weathering of Mn-rich carbonates or silicates by *in situ* oxidation or dissolution-
332 reprecipitation (Glasby 2006; Nicholson et al. 1997; Post 1999). In deep sea water, Mn nodules
333 generally appear in oxygenated environments as concentric layers of Mn and Fe oxides around other
334 minerals such as carbonate mineral fragments, pumice shards, animal remains, and coral fragments
335 (Glasby 2000; Von Damm 1990). Our thermodynamic study suggests that, as manganese minerals
336 undergo dissolution and precipitation at the anoxic - oxic interface of aqueous geochemical
337 environments, both low oxygen fugacity and large grain size thermodynamically favor carbonate
338 formation. The surface energy effects described here thus explain the formation of $MnCO_3$ as coarse
339 grains in the anaerobic geochemical environments (Pedersen and Price 1982) and are relevant to the
340 formation of manganese oxide minerals as fine grained minerals in soils, sediments and Mn nodules in
341 deep sea floor and crusts (Glasby 2006; Glasby 2000; Post 1999). The size driven thermodynamic
342 effects also explain the appearance of thin films of haumannite (Mn_3O_4) as a nanophase on the

343 rhodochrosite surface at an anoxic - oxic interface (Kendall et al. 2008; Na et al. 2007; Na and Martin
344 2009).

345 Recent evaluations of different geologic environments for CO_2 sequestration show relatively
346 faster precipitation of carbonate minerals in basalts compared to other silicate rocks (Sturmer et al.
347 2007). In addition to other common carbonates, manganese carbonate formation seems to contribute
348 to carbonation reactions of basalt with Mn bearing minerals. The phase equilibrium studies in this
349 work predict the expanded stability field for $MnCO_3$ in supercritical (sc) CO_2 both in hydrous and
350 anhydrous media. This also explains the enhanced carbonation reaction on the addition of H_2S to
351 $scCO_2$–H_2O due to reduction and dissolution of Fe (III) or Mn (III, IV) minerals present in the basaltic
352 rocks (Schaef et al. 2009; Schaef et al. 2010).

353 Earlier thermodynamic studies have shown that low surface energy oxides with weakly bound
354 water are better water oxidation catalysts (Mn oxides, (Birkner et al. 2013), sensors (tin oxide, (Ma et
355 al. 2011) and Li-ion exchange ($LiCoO_2$, Maram et al. 2013) than phases with larger surface energies
356 and more strongly bound water. The low surface energy and weaker binding sites of $MnCO_3$ that allow
357 easier exchange of adsorbed molecules could be the possible reason for the development of $MnCO_3$
358 nano/microspheres for drug delivery, biosensing (Peng et al. 2011; Qi et al. 2010; Wang et al., 2009;
359 Zhang et al., 2009) and reversible lithium storage applications (Aragón et al., 2007, 2011;
360 Mirhashemihaghighi et al. 2012). Interestingly, the delithiated microporous manganese carbonate form
361 X-ray amorphous carbonate phase on Li re-intercalation. This phase has not been well characterized
362 and could be a metastable amorphous manganese carbonate phase similar to AMnC in the present
363 study. Thus AMnC could provide a low energy pathway for manganese carbonate formation during
364 the electrochemical process as well. Electrochemical study of AMnC itself as a starting anode material
365 would be interesting and this could also eliminate possible material compatibility issues due to any

366 volume change arising from the nanocrystalline to amorphous phase transformation during $MnCO_3$
367 electrochemical cycling.

368 Furthermore, both manganese oxides and manganese carbonate may have catalytic activity in
369 the natural environment, may participate in biogeochemical cycles, and may even have provided
370 catalytic environments in prebiotic organic chemistry and the origin of life. The changes in
371 thermodynamic, surface, and electrochemical properties associated with nanophase and amorphous
372 manganese carbonates may be important in these contexts as well.

373

374 **ACKNOWLEDGEMENTS**

375 This work is supported as part of the Center for Nanoscale Control of Geologic CO_2, an Energy
376 Frontier Research Center funded by the U.S. Department of Energy, Office of Science, Office of Basic
377 Energy Sciences under Award Number DE-AC02-05CH11231. The authors thank Tien Tran for help
378 with SEM.

379

380

Table 1. The water content and calorimetric data of amorphous manganese carbonate (AMnC) samples.

Amorphous $MCO_3 \cdot nH_2O$	**Water (n) (mol) (TGA)**	**Enthalpy of Crystallization (ΔH_{crys}) (kJ/mol)**	**Ionic/ crystal radius M^{2+} (nm)[e]**
$MnCO_3.nH_2O$ (AMnC-I)[a]	1.2 ± 0.04	-32.44± 0.71	0.083 (0.097)
$MnCO_3.nH_2O$ (AMnC-II)[a]	1.78 ± 0.19	-31.62 ± 0.82	
$CaCO_3.nH_2O$ (ACC)[b]	1.13 - 1.58	-17 ± 1 to -24 ± 1	0.1 (0.114)
$MgCO_3.nH_2O$ (AMC)[c]	1.28	-35.8 ± 1.2	0.072 (0.086)
$FeCO_3.nH_2O$ (AFC)[d]	1.75	-37.8 ± 9.8	0.078 (0.092)

The values in () is crystal radius.
a This work
b (Radha et al., 2010)
c (Radha et al., 2012)
d (Sel et al., 2012)
e http://abulafia.mt.ic.ac.uk/shannon/ptable.php

401 Table 2. The water content, particle size analysis and calorimetric data of nanophase manganese carbonate (NMnC) samples.

Sample ID $MnCO_3 \cdot nH_2O$	Precipitate aging condition	nH_2O (mol)		Surface area BET (m^2/mol)	ΔH_{soln} (KJ/mol)	$\Delta H_{corr\text{-}H2O}$ (KJ/mol)		XRD Crystallite size (nm)	BET Particle size (nm)	SEM Particle size (nm)
		Total	chemi			physi	chemi			
NMnC-1	5 min at 25 °C	0.79 ± 0.04	0.145± 0.04	9712 ± 28	-25.5 ± 0.6	-25.2 ± 0.6	-28.4 ± 1.3	9.1 ± 0.4	19.2 ± 0.08	32 ± 2
NMnC-2	5.0 h at 25 °C	0.51 ± 0.01	0.121± 0.01	8073± 230	-22.6 ± 0.8	-22.3 ± 0.8	-24.96 ± 1.3	28 ± 3	23.1 ± 0.7	92 ± 8
NMnC-3	1.0 h at 25 °C	0.39 ± 0.02	0.074± 0.02	4927 ± 38	-22.9 ± 0.5	-22.8 ± 0.5	-24.4 ± 0.9	28 ± 1.7	37.8 ± 0.3	96 ± 4
NMnC-4	1.0 h at 85 °C	0.12 ± 0.01	0.070± 0.01	4698 ± 60	-21.0 ± 0.5	-20.99 ± 0.5	-22.52 ± 0.95	38.6 ± 1.8	39.7 ± 0.6	97 ± 8
NMnC-5	2.5h at 25 °C	0.35 ± 0.02	0.047± 0.02	3168 ± 138	-20.3 ± 0.9	-20.1 ± 0.9	-21.1 ± 1.1	34.0 ± 1.8	58.8 ± 2.8	86 ± 10
NMnC-6	2.5 h at 85 °C	0.09 ± 0.02	0.063± 0.02	4232 ± 253	-21.1 ± 0.9	-21.0 ± 0.9	-22.41 ± 1.1	35.9 ± 1.9	44.0 ± 5.1	78 ± 9
NMnC-7	HT at160 °C	0.02 ± 0.01	0.013± 0.01	857 ± 23	-19.2 ± 0.4	-19.2 ± 0.4	-19.5 ± 0.5	58.9 ± 3	217.5 ± 6.5	144 ± 10

402

403

404 ΔH_{soln} = enthalpy of solution; $\Delta H_{sol\text{-}corr;\ nano}$ = enthalpy corrected for water as physically (physi) and chemically (chmi) adsorbed

405

406

407

Table 3. Thermochemical cycles used to calculate of crystallization enthalpy (ΔH_{crys}) of amorphous manganese carbonate (AMnC) and surface energies of nanophase $MnCO_3$ (NMnC).

.

I – Crystallization enthalpy of AMnC (ΔH_{crys})

$MnCO_3 \cdot nH_2O_{(amr,\ 26\ ^oC)} + 2\ HCl_{(soln,\ 26\ ^oC)} \rightarrow Mn^{2+}_{(soln,\ 26\ ^oC)} + CO_{2\ (g,\ 26\ ^oC)} + (1+ n)\ H_2O_{(soln,\ 26\ ^oC)} + 2Cl^-_{(soln,\ 26\ ^oC)}$ $\Delta H_1 = \Delta H_{soln(amorphous)}$

$H_2O_{(l,\ 26\ ^oC)} \rightarrow H_2O_{(soln,\ 26\ ^oC)}$ ΔH_2 = -0.4 kJ/mol (Parker, 1965)

$MnCO_{3\ (xl,\ 26\ ^oC)} + 2\ HCl_{(soln,\ 26\ ^oC)} \rightarrow Mn^{2+}_{(soln,\ 26\ ^oC)} + CO_{2\ (g,\ 26\ ^oC)} + 2\ Cl^-_{(soln,\ 26\ ^oC)}\ H_2O_{(sln,\ 298\ K)}$ $\Delta H_3 = \Delta H_{soln\text{-}rhodochrosite}$

$MnCO_3 \cdot nH_2O_{(amrorphous,\ 298\ K)} = MnCO_{3\ (rhodochrosite,\ 26\ ^oC)} + n\ H_2O_{(26\ ^oC)}$ $\Delta H_4 = \Delta H_{trns}$

$$\Delta H_4 = \Delta\ H_1 - n\ \Delta H_2 - \Delta H_3$$

II - Correction for liquid water (NMnC hydrous surface) ($\Delta H_{sol\text{-}corr\text{-}physi}$)

$MnCO_3 \bullet n\ H_2O_{(xl,\ 298\ K)} + 2\ HCl_{(sln,\ 298\ K)} \rightarrow Mn^{2+}_{(sln,\ 298\ K)} + CO_{2\ (g,\ 298\ K)} + (1+ n)\ H_2O_{(sln,\ 298\ K)} + 2\ Cl^-_{(sln,\ 298\ K)}$ $\Delta H_1 = \Delta H_{sol}$

H_2O (l, 298 K) $\rightarrow H_2O$ (sln, 298 K) ΔH_2 = -0.4 kJ/mol (Parker, 1965)

$MnCO_{3\ (xl,\ 298\ K)} + 2\ HCl_{(sln,\ 298\ K)} \rightarrow Mn^{2+}_{(sln,\ 298\ K)} + CO_{2\ (g,\ 298K)} + 2\ Cl^-_{(sln,\ 298\ K)} + H_2O_{(sln,\ 298\ K)}$ $\Delta H_4 = \Delta H_{sol\text{-}corr\text{-}physi}$

$$\Delta H_4 = \Delta\ H_1 - n\ \Delta H_2$$

III - Correction for chemisorbed liquid water (NMnC anhydrous surface)($\Delta H_{sol\text{-}corr\text{-}chem}$)

$MnCO_3 \bullet nH_2O_{(xl,\ 298\ K)} + 2\ HCl_{(sln,\ 298\ K)} \rightarrow Mn^{2+}_{(sln,\ 298\ K)} + CO_{2(g,\ 298\ K)} + (1+ n)\ H_2O_{(sln,\ 298\ K)} + 2\ Cl^-_{(sln,\ 298\ K)}$ $\Delta H_1 = \Delta H_{sol}$

$H_2O_{(l,\ 298\ K)} \rightarrow H_2O_{(sln,\ 298\ K)}$ ΔH_2 = -0.4 kJ/mol (Parker, 1965)

$H_2O_{(chemi\text{-}ads,\ 298\ K)} \rightarrow H_2O_{(liq,\ 298\ K)}$ $\Delta H_3 = (\Delta H_{chemads\text{-}liq}) = 43.02 \pm 0.79$ kJ/mol

$MnCO_{3(xl,\ 298\ K)} + 2\ HCl_{(sln,\ 298\ K)} \rightarrow Mn^{2+}_{(sln,\ 298\ K)} + CO_{2(g,\ 298K)} + 2\ Cl^-_{(sln,\ 298\ K)} + H_2O_{(sln,\ 298\ K)}$ $\Delta H_4 = \Delta H_{sol\text{-}corr\text{-}chem}$

$$\Delta H_4 = \Delta\ H_1 - n\ \Delta H_2 - (n\text{-}x)\ \Delta H_3$$

IV - Enthalpy of conversion from NMnC to bulk ($\Delta H_{nano \rightarrow bulk}$)

$MnCO_{3\ (xl,\ bulk,\ 298\ K)} + 2\ HCl_{(sln,\ 298\ K)} \rightarrow Mn^{2+}_{(sln,\ 298\ K)} + CO_{2\ (g,\ 298K)} + 2\ Cl^-_{(sln,\ 298\ K)} + H_2O_{(sln,\ 298\ K)}$ $\Delta H_5 = \Delta H_{sol\text{-}cor,\ bulk}$

$MnCO_{3\ (xl,\ nano\ 298\ K)} + 2\ HCl_{(sln,\ 298\ K)} \rightarrow Mn^{2+}_{(sln,\ 298\ K)} + CO_{2\ (g,\ 298K)} + 2\ Cl^-_{(sln,\ 298\ K)} + H_2O_{(sln,\ 298\ K)}$ $\Delta H_6 = \Delta H_{sol\text{-}cor,\ nano}$

$MnCO_{3\ (xl,\ nano,\ 298K)} \rightarrow MnCO_{3\ (xl,\ bulk,\ 298\ K)}$ ΔH_7 = and $\Delta H_{nano \rightarrow bulk}$

$$\Delta H_7 = \Delta H_6 - \Delta H_5$$

441

442 **List of Figure Captions**

443

444 Figure 1. Powder XRD patterns of (a) amorphous manganese carbonate (AMnC) and (b) nanophase
445 manganese carbonate (NMnC) samples.

446

447 Figure 2. Differential enthalpies of water adsorption on nanophase manganese carbonate as a function
448 of surface coverage (H_2O per nm^2).

449

450 Figure 3. The solution enthalpies for the water-corrected rhodochrosite samples plotted against the
451 surface area obtained by BET analysis for (a) hydrous surface and (b) anhydrous surface.

452

453 Figure 4. The Eh(pE)-pH diagrams of $Mn_3O_4/MnCO_3$ for bulk and nano (10 nm) phases with aqqeous
454 Mn species ($[Mn^{2+}] = 10^{-6}$). (a) P_{CO2} at normal sea level air ($P_{CO2} = 10^{-3.5}$, T = 25 °C) and (b) in
455 supercritical CO_2 (P_{CO2} = 72.9 atm, T = 31.25 °C). Reactions 2 and 3 are given in Table 5.

456

457 Figure 5. The oxygen-CO_2 fugacity diagrams for bulk and nanophase (10 nm) $Mn_2O_3/MnCO_3$ system
458 at 25 and 100 °C for equilibrium reaction 6 $MnCO_{3(s)}$ + O_2 → 2 $Mn_3O_{4\ (s)}$ + 6 $CO_{2(g)}$

459

460 **References:**

461 Aragón, M.J., León, B., Pérez Vicente, C., and Tirado, J.L. (2011) A new form of manganese
462 carbonate for the negative electrode of lithium-ion batteries. Journal of Power Sources, 196(5),
463 2863-2866.
464 Aragón, M.J., Pérez-Vicente, C., and Tirado, J.L. (2007) Submicronic particles of manganese
465 carbonate prepared in reverse micelles: A new electrode material for lithium-ion batteries.
466 Electrochemistry Communications, 9(7), 1744-1748.
467 Bewernitz, M.A., Gebauer, D., Long, J., Colfen, H., and Gower, L.B. (2012) A metastable liquid
468 precursor phase of calcium carbonate and its interactions with polyaspartate. Faraday
469 Discussions, 159, 291-312.
470 Birkner, N., and Navrotsky, A. (2012) Thermodynamics of manganese oxides: effects of particle size
471 and hydration on oxidation-reduction equilibria among hausmannite, bixbyite, and pyrolusite.
472 American Mineralogist, 97(8-9), 1291-1298.
473 Birkner, N., Nayeri, S., Pashaei, B., Najafpour, M.M., Casey, W.H., and Navrotsky, A. (2013)
474 Energetic basis of catalytic activity of layered nanophase calcium manganese oxides for water
475 oxidation. Proc. Natl. Acad. Sci. U. S. A., Early Ed.(Copyright (C) 2013 American Chemical
476 Society (ACS). All Rights Reserved.), 1-6, 6 pp.
477 Bourg, A.C.M., and Bertin, C. (1994) Seasonal and Spatial Trends in Manganese Solubility in an
478 Alluvial Aquifer. Environmental Science & Technology, 28(5), 868-876.
479 Capobianco, C., and Navrotsky, A. (1987) Solid-solution thermodynamics in $CaCO_3$-MnCO3.
480 American Mineralogist, 72(3-4), 312-8.
481 Cui, L., Niu, M., Chen, G., and Wang, Y. (2009) Fabrication and structure characterization of
482 MnCO3/Î±-Fe2O3 nanocrystal heterostructures. Materials Letters, 63(28), 2499-2502.
483 De Yoreo, J.J., and Vekilov, P.G. (2003) Principles of crystal nucleation and growth. Reviews in
484 Mineralogy & Geochemistry, 54(Biomineralization), 57-93.
485 De Yoreo, J.J., Wierzbicki, A., and Dove, P.M. (2007) New insights into mechanisms of biomolecular
486 control on growth of inorganic crystals. CrystEngComm, 9(12), 1144-1152.
487 De Yoreo, J.J., Zepeda-Ruiz, L.A., Friddle, R.W., Qiu, S.R., Wasylenki, L.E., Chernov, A.A., Gilmer,
488 G.H., and Dove, P.M. (2009) Rethinking Classical Crystal Growth Models through Molecular
489 Scale Insights: Consequences of Kink-Limited Kinetics. Crystal Growth & Design, 9(12),
490 5135-5144.
491 Duckworth, O.W., Cygan, R.T., and Martin, S.T. (2004) Linear free energy relationships between
492 dissolution rates and molecular modeling energies of rhombohedral carbonates. Langmuir,
493 20(7), 2938-2946.
494 Fernandez-Martinez, A., Kalkan, B., Clark, S.M., and Waychunas, G.A. (2013) Pressure-Induced
495 Polyamorphism and Formation of 'Aragonitic' Amorphous Calcium Carbonate. Angewandte
496 Chemie International Edition, 52(32), 8354-8357.
497 Fischer, T.B., Heaney, P.J., Jang, J.-H., Ross, D.E., Brantley, S.L., Post, J.E., and Tien, M. (2008)
498 Continuous time-resolved X-ray diffraction of the biocatalyzed reduction of Mn oxide. Am.
499 Mineral., 93(11-12), 1929-1932.
500 Forbes, T.Z., Radha, A.V., and Navrotsky, A. (2011) The energetics of nanophase calcite. Geochimica
501 et Cosmochimica Acta, 75(24), 7893-7905.

Frankel, R.B., and Bazylinski, D.A. (2003) Biologically induced mineralization by bacteria. Rev. Mineral. Geochem., 54(Biomineralization), 95-114.

Gebauer, D., and Coelfen, H. (2011) Prenucleation clusters and non-classical nucleation. Nano Today, 6(6), 564-584.

Gebauer, D., Voelkel, A., and Coelfen, H. (2008) Stable Prenucleation Calcium Carbonate Clusters. Science (Washington, DC, U. S.), 322(5909), 1819-1822.

Gingele, F.X., and Kasten, S. (1994) Solid-phase manganese in Southeast Atlantic sediments: Implications for the paleoenvironment. Mar. Geol., 121(3/4), 317-32.

Glasby, G. (2006) Manganese: Predominant Role of Nodules and Crusts. In H. Schulz, and M. Zabel, Eds. Marine Geochemistry, p. 371-427. Springer Berlin Heidelberg.

Glasby, G.P. (2000) Manganese: predominant role of nodules and crusts, p. 335-372. Springer-Verlag.

Goldsmith, J.R., and Graf, D.L. (1957) The system CaO-MnO-CO_2: Solid-solution and decomposition relations. Geochimica et Cosmochimica Acta, 11(4), 310-334.

Goren, O., Lazar, B., Burg, A., and Gavrieli, I. (2012) Mobilization and retardation of reduced manganese in sandy aquifers: Column experiments, modeling and implications. Geochimica et Cosmochimica Acta, 96(0), 259-271.

Hu, Q., Nielsen, M.H., Freeman, C.L., Hamm, L.M., Tao, J., Lee, J.R.I., Han, T.Y.J., Becker, U., Harding, J.H., Dove, P.M., and De Yoreo, J.J. (2012) The thermodynamics of calcite nucleation at organic interfaces: Classical vs. non-classical pathways. Faraday Discussions, 159, 509-523.

Katsikopoulos, D., Fernández-González, Ã.N., and Prieto, M. (2009) Precipitation and mixing properties of the "disordered" (Mn,Ca)CO_3 solid solution. Geochimica et Cosmochimica Acta, 73(20), 6147-6161.

Kendall, T.A., Na, C., Jun, Y.-S., and Martin, S.T. (2008) Electrical Properties of Mineral Surfaces for Increasing Water Sorption. Langmuir, 24(6), 2519-2524.

Koga, N., Nakagoe, Y., and Tanaka, H. (1998) Crystallization of amorphous calcium carbonate. Thermochimica Acta, 318(1-2), 239-244.

Ma, Y., Castro, R.H.R., Zhou, W., and Navrotsky, A. (2011) Surface enthalpy and enthalpy of water adsorption of nanocrystalline tin dioxide: thermodynamic insight on the sensing activity. J. Mater. Res., 26(Copyright (C) 2013 American Chemical Society (ACS). All Rights Reserved.), 848-853.

Maram, P.S., Costa, C.C.G., Navrotsky, A. (2013) Experimental Confirmation of Low Surface Energy in $LiCoO_2$ and Implications for Lithium Battery Electrodes. Angewandte Chemie International Edition 52(46), 12139-12142.

McBeath, M.K., Rock, P.A., Casey, W.H., and Mandell, G.K. (1998) Gibbs energies of formation of metal-carbonate solid solutions: part 3. The $Ca_xMn_{1-x}CO_3$ system at 298 K and 1 bar. Geochimica et Cosmochimica Acta, 62(16), 2799-2808.

Mirhashemihaghighi, S., León, B., Pérez Vicente, C., Tirado, J.L., Stoyanova, R., Yoncheva, M., Zhecheva, E., Sáez Puche, R., Arroyo, E.M., and Romero de Paz, J. (2012) Lithium Storage Mechanisms and Effect of Partial Cobalt Substitution in Manganese Carbonate Electrodes. Inorganic Chemistry, 51(10), 5554-5560.

Na, C., Kendall, T.A., and Martin, S.T. (2007) Surface-potential heterogeneity of reacted calcite and rhodochrosite. Environmental Science & Technology, 41(18), 6491-6497.

Na, C., and Martin, S.T. (2009) Growth of Manganese Oxide Nanostructures Alters the Layout of Adhesion on a Carbonate Substrate. Environmental Science & Technology, 43(13), 4967-4972.

Navrotsky, A. (2009) Energetics of oxide nanoparticles. International Journal of Quantum Chemistry, 109(12), 2647-2657.

Navrotsky, A. (2011) Nanoscale Effects on Thermodynamics and Phase Equilibria in Oxide Systems. Chemphyschem, 12(12), 2207-2215.

Navrotsky, A., Ma, C., Lilova, K., and Birkner, N. (2010) Nanophase Transition Metal Oxides Show Large Thermodynamically Driven Shifts in Oxidation-Reduction Equilibria. Science (Washington, DC, United States), 330(6001), 199-201.

Nicholson, K., Hein, J.R., Buehn, B., Dasgupta, S., and Editors. (1997) Manganese Mineralization: Geochemistry and Mineralogy of Terrestrial and Marine Deposits. [In: Geol. Soc. Spec. Publ., 1997; 119]. 370 pp. p. Geol Soc Publ House.

Parker, V.B. (1965) Thermal properties of uni-univalent electrolytes. National Standard Reference Data Series, 2, p. 66. National Bureau of Standards.

Pedersen, T.F., and Price, N.B. (1982) The geochemistry of manganese carbonate in Panama Basin sediments. Geochimica et Cosmochimica Acta, 46(1), 59-68.

Peng, J., Feng, L.-N., Zhang, K., Li, J.-J., Jiang, L.-P., and Zhu, J.-J. (2011) Multifunctional Manganese Carbonate Microspheres with Superparamagnetic and Fluorescent Properties: Synthesis and Biological Application. Chemistry – A European Journal, 17(39), 10916-10923.

Post, J.E. (1999) Manganese oxide minerals: Crystal structures and economic and environmental significance. Proceedings of the National Academy of Sciences, 96(7), 3447-3454.

Qi, W., Wang, A., Yang, Y., Du, M., Bouchu, M.N., Boullanger, P., and Li, J. (2010) The lectin binding and targetable cellular uptake of lipid-coated polysaccharide microcapsules. Journal of Materials Chemistry, 20(11), 2121-2127.

Radha, A.V., Fernandez-Martinez, A., Hu, Y., Jun, Y.-S., Waychunas, G.A., and Navrotsky, A. (2012) Energetic and structural studies of amorphous $Ca_{1-x}Mg_xCO_3 \cdot nH_2O$ ($0 \leq x \leq 1$). Geochimica et Cosmochimica Acta, 90, 83-95.

Radha, A.V., Forbes, T.Z., Killian, C.E., Gilbert, P.U.P.A., and Navrotsky, A. (2010) Transformation and crystallization energetics of synthetic and biogenic amorphous calcium carbonate. Proceedings of the National Academy of Sciences of the United States of America, 107(38), 16438-16443.

Railsback, L.B. (1999) Patterns in the compositions, properties, and geochemistry of carbonate minerals. Carbonates and Evaporites, 14(1), 1-20.

Raiteri, P., and Gale, J.D. (2010) Water is the key to nonclassical nucleation of amorphous calcium carbonate. J Am Chem Soc, 132(49), 17623-34.

Schaef, H.T., McGrail, B.P., and Owen, A.T. (2010) Carbonate mineralization of volcanic province basalts. International Journal of Greenhouse Gas Control, 4(2), 249-261.

Schaef, H.T., McGrail, B.P., and Owen, A.T. (2009) Basalt- CO_2-H_2O interactions and variability in carbonate mineralization rates. Energy Procedia, 1(1), 4899-4906.

Seguin, M.K. (1972) Stability of manganese carbonate in inert atmospheres and in air. Amer. Mineral., 57(Copyright (C) 2013 American Chemical Society (ACS). All Rights Reserved.), 511-23.

Sel, O., Radha, A.V., Dideriksen, K., and Navrotsky, A. (2012) Amorphous iron (II) carbonate: Crystallization energetics and comparison to other carbonate minerals related to CO2 sequestration. Geochimica et Cosmochimica Acta, 87, 61-68.

Smith, S.J., Stevens, R., Liu, S., Li, G., Navrotsky, A., Boerio-Goates, J., and Woodfield, B.F. (2009) Heat capacities and thermodynamic functions of TiO2 anatase and rutile: analysis of phase stability. Am. Mineral., 94(Copyright (C) 2013 American Chemical Society (ACS). All Rights Reserved.), 236-243.

Sternbeck, J. (1997) Kinetics of rhodochrosite crystal growth at 25 °C: The role of surface speciation. Geochimica et Cosmochimica Acta, 61(4), 785-793.

Sturmer, D.M., LaPointe, D.D., Price, J.G., Hess, R.H. (2007) Assessment of the potential for carbon dioxide sequestration by reactions with rocks in Nevada. Mackay School of Earth Sciences and Engineering, College of Science, University of Nevada, Reno, Reno, Nev.

Takahara, I., Murata, K., Sato, K., Miura, Y., Inaba, M., and Liu, Y. (2012) Activity and deactivation nature of Ru/$MnCO_3$ catalysts for Fischer-Tropsch reaction reaction. Applied Catalysis A: General, 450(0), 80-87.

Tribello, G.A., Bruneval, F., Liew, C.C., and Parrinello, M. (2009) A Molecular Dynamics Study of the Early Stages of Calcium Carbonate Growth. Journal of Physical Chemistry B, 113(34), 11680-11687.

Von Damm, K.L. (1990) Seafloor Hydrothermal Activity: Black Smoker Chemistry and Chimneys. Annual Review of Earth and Planetary Sciences, 18(1), 173-204.

Wallace, A.F., Hedges, L.O., Fernandez-Martinez, A., Raiteri, P., Gale, J.D., Waychunas, G.A., Whitelam, S., Banfield, J.F., and De Yoreo, J.J. (2013) Microscopic Evidence for Liquid-Liquid Separation in Supersaturated CaCO3 Solutions. Science, 341(6148), 885-889.

Wang, L., Vu, K., Navrotsky, A., Stevens, R., Woodfield, B.F., and Boerio-Goates, J. (2004) Calorimetric Study: Surface Energetics and the Magnetic Transition in Nanocrystalline CoO. Chem. Mater., 16(Copyright (C) 2013 American Chemical Society (ACS). All Rights Reserved.), 5394-5400.

Wang, Q., Grau-Crespo, R., and de Leeuw, N.H. (2011) Mixing Thermodynamics of the Calcite-Structured (Mn,Ca)CO3 Solid Solution: A Computer Simulation Study. The Journal of Physical Chemistry B, 115(47), 13854-13861.

Wang, W., and Ao, L. (2007) Synthesis and Optical Properties of Mn_3O_4 Nanowires by Decomposing MnCO3 Nanoparticles in Flux. Crystal Growth & Design, 8(1), 358-362.

Wang, Y., Price, A.D., and Caruso, F. (2009) Nanoporous colloids: building blocks for a new generation of structured materials. Journal of Materials Chemistry, 19(36), 6451-6464.

Wolf, S.E., Muller, L., Barrea, R., Kampf, C.J., Leiterer, J., Panne, U., Hoffmann, T., Emmerling, F., and Tremel, W. (2011) Carbonate-coordinated metal complexes precede the formation of liquid amorphous mineral emulsions of divalent metal carbonates. Nanoscale, 3(3), 1158-1165.

Yang, L.-X., Zhu, Y.-J., Tong, H., and Wang, W.-W. (2007) Submicrocubes and highly oriented assemblies of $MnCO_3$ synthesized by ultrasound agitation method and their thermal transformation to nanoporous Mn_2O_3. Ultrasonics Sonochemistry, 14(2), 259-265.

Zhang, R., Lu, D., Lin, Z., Li, L., Jin, W., and Mohwald, H. (2009) Enriched encapsulation and fluorescence enhancement of europium complexes in microcapsules. Journal of Materials Chemistry, 19(10), 1458-1463.

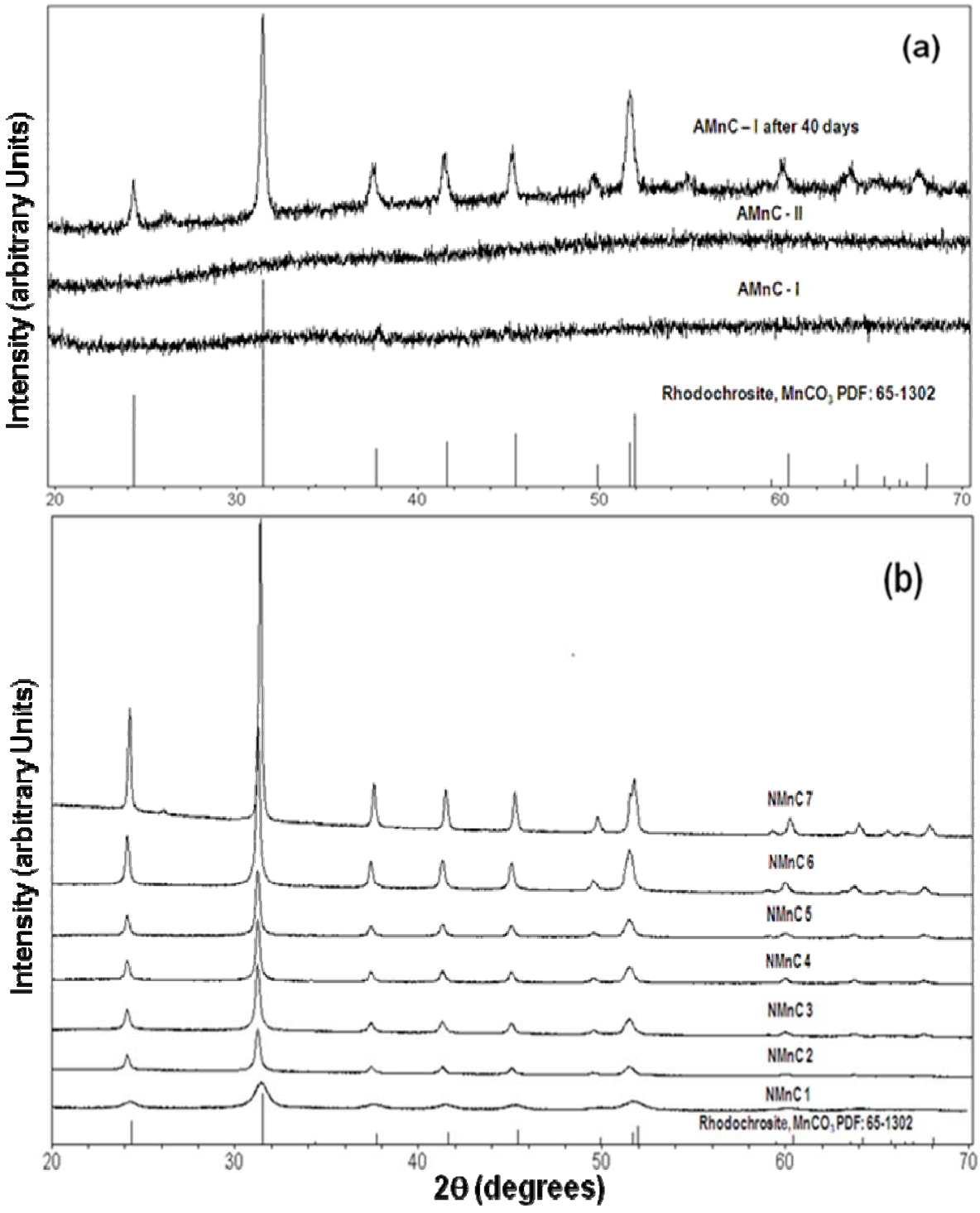

631

632 Figure 1

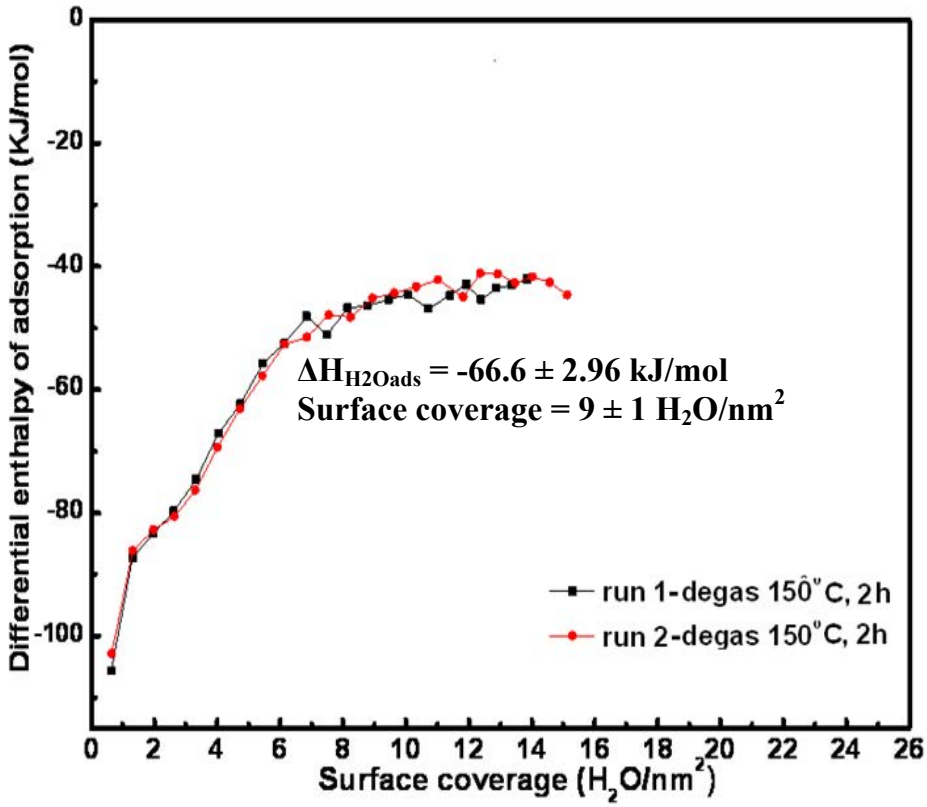

633

634

635

636 Figure 2

637

638

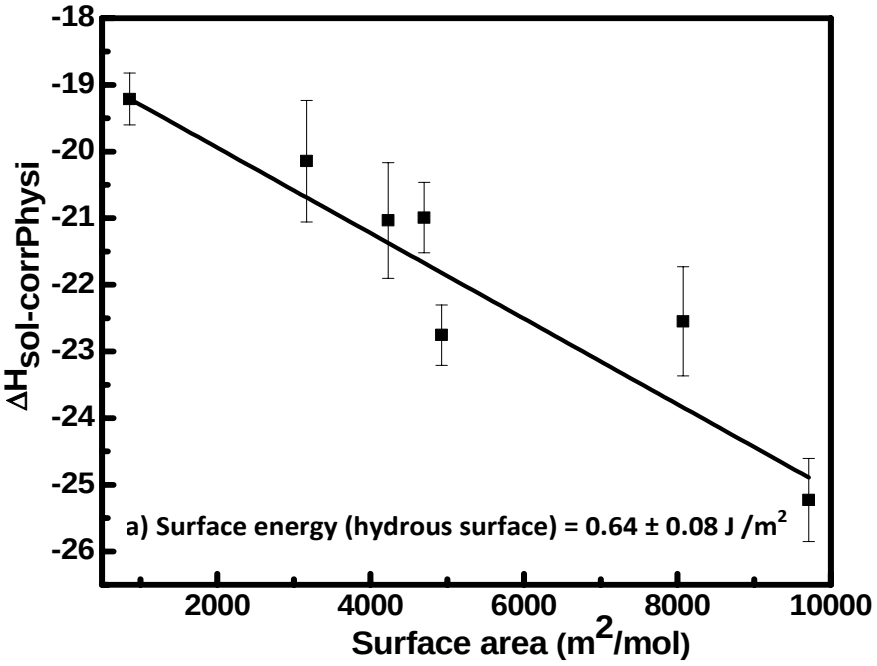

639

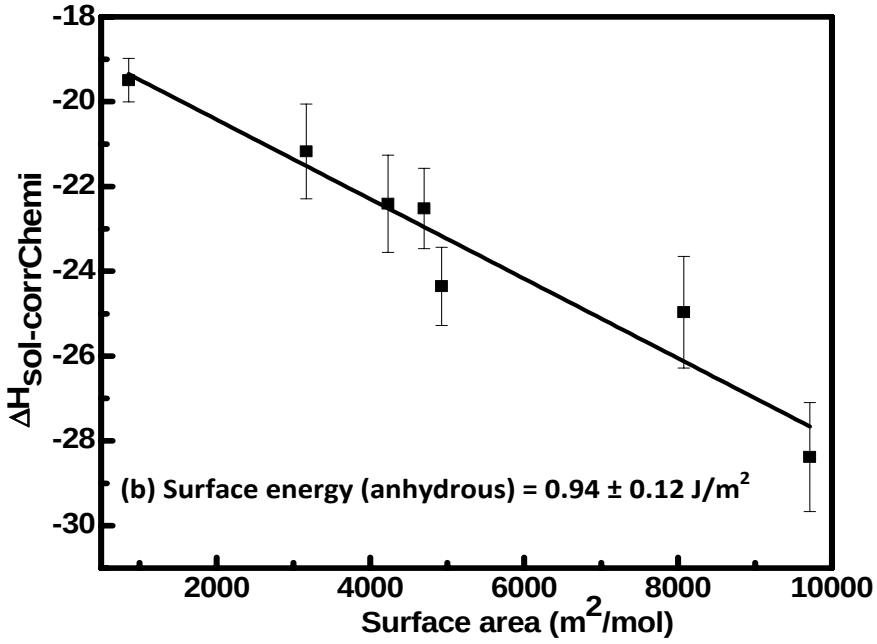

640

641 Figure 3

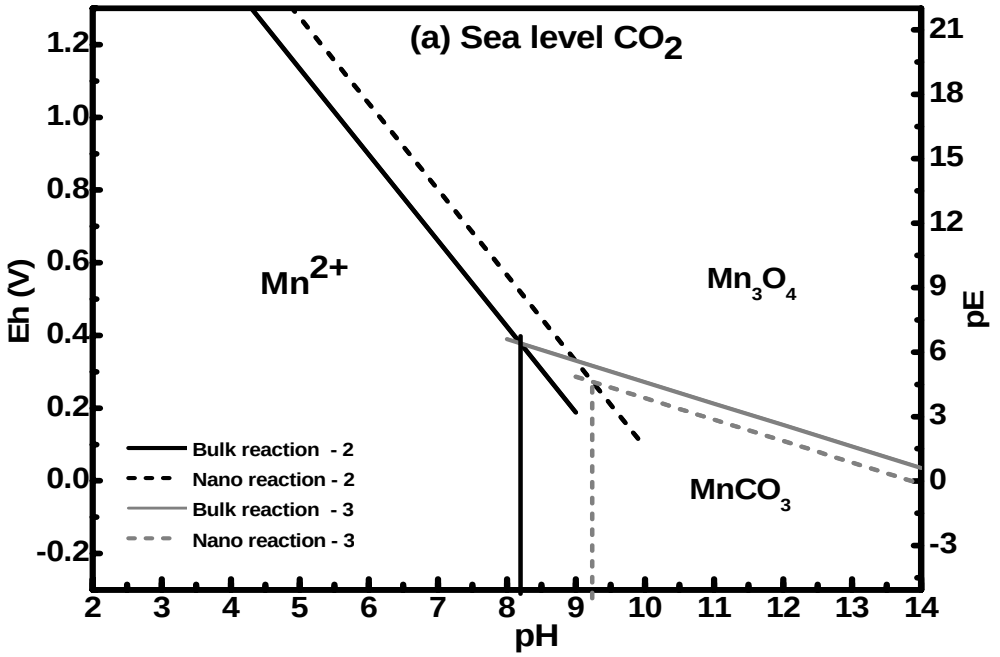

642

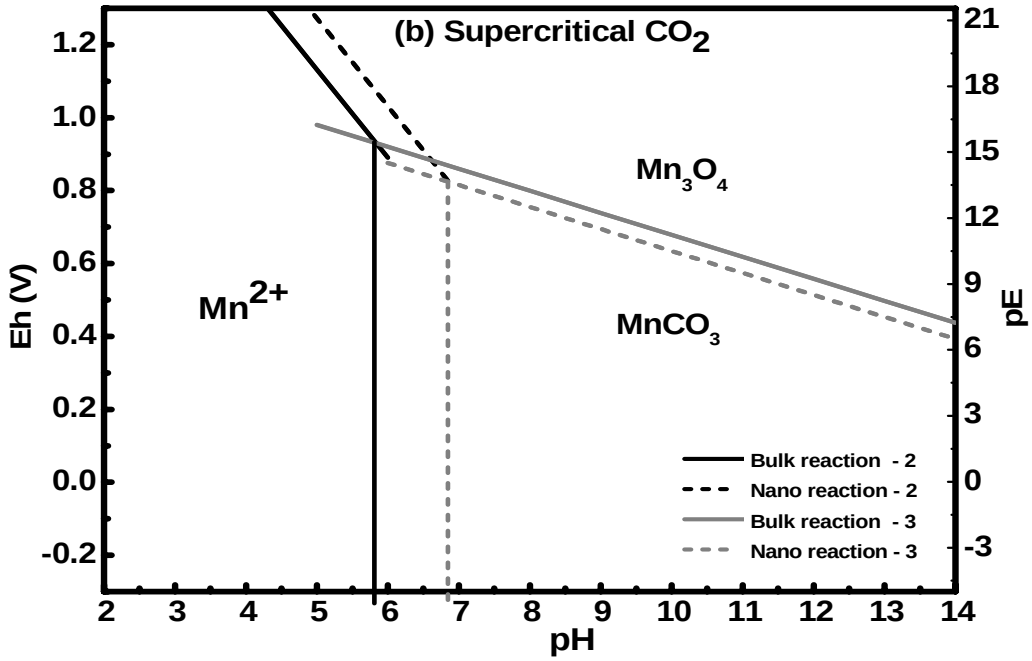

643

644 Figure 4

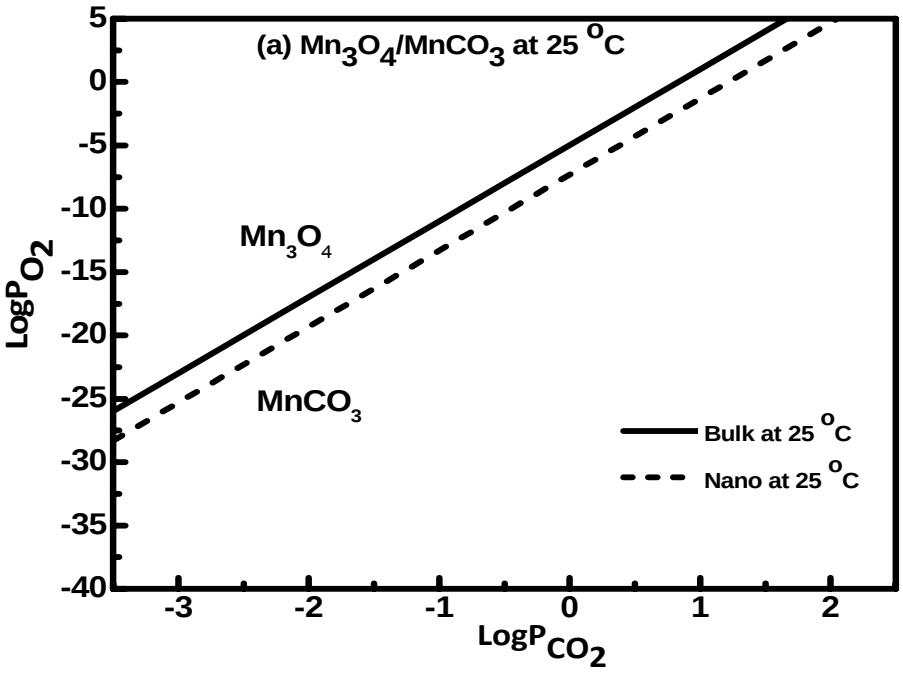

645

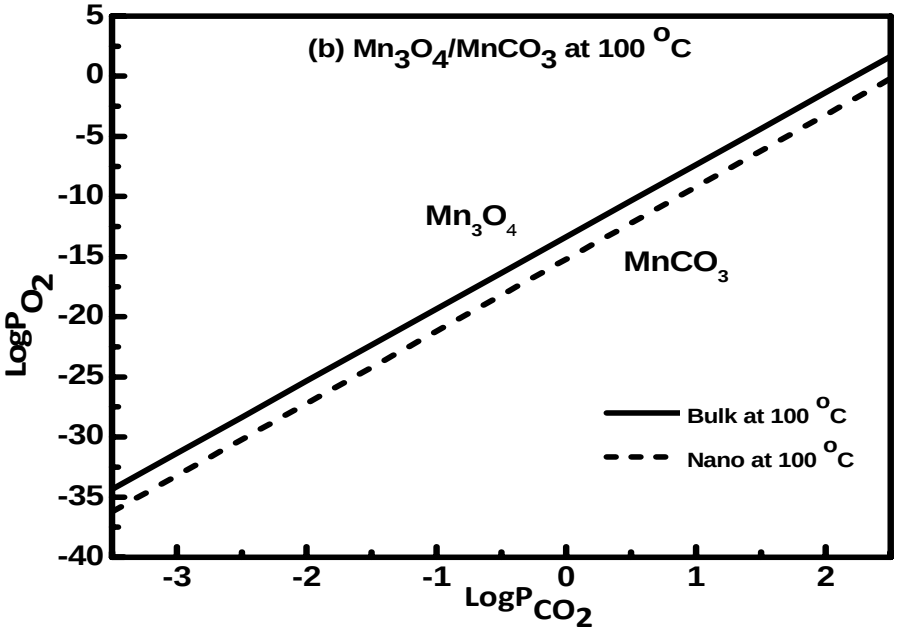

646

647 Figure 5

648